Electronic Supplementary Material (ESI) for Energy & Environmental Science.

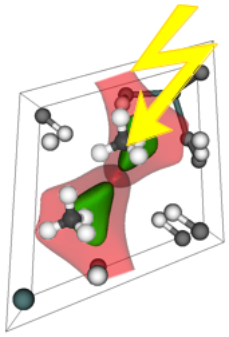

Supplementary Information

The Materials Genome in Action: Identifying the Performance Limits for Methane Storage

Cory M. Simon, Jihan Kim, Diego A. Gomez-Gualdron, Jeffrey S. Camp, Yongchul G. Chung, Richard L. Martin, Rocio Mercado, Michael Deem, Dan Gunter, Maciej Haranczyk, David S. Sholl, Randall Q. Snurr, Berend Smit

December 19, 2014

S1 Screening the database

Fig. S1 gives a scatter plot of the deliverable capacity of the training set against the largest included sphere. The structures with the highest deliverable capacities have largest included spheres that fall in $[8.0, 14.5\text{Å}]$, shown as the interval bracketed by the blue, vertical lines. The color-coding of the points in Fig. S1 indicates the void fraction. As all green points have void fractions outside of $[0.25, 0.7]$, we see that the structures with the highest deliverable capacities also have void fractions in the interval $[0.25, 0.7]$.

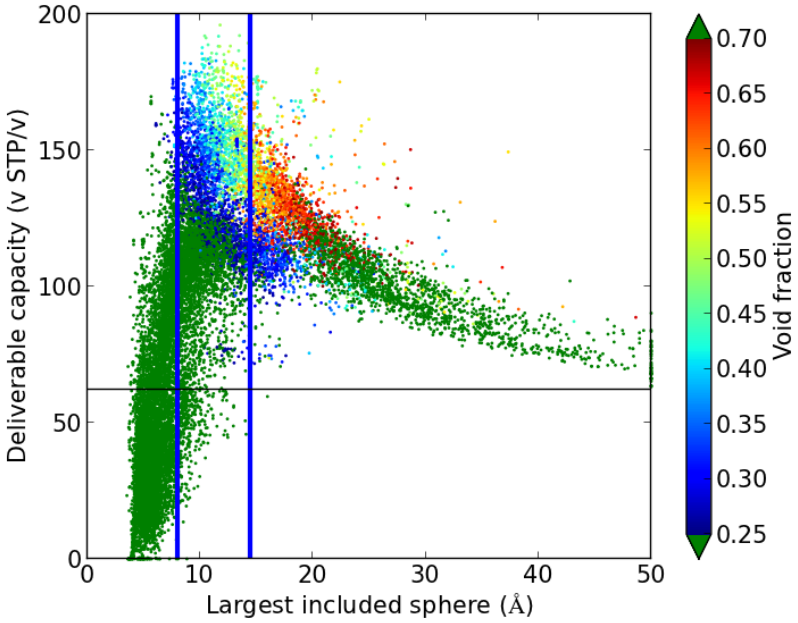

Figure S1. Screening strategy with geometric descriptors. Deliverable capacity plotted against the diameter of the largest included sphere. Color indicates geometric void fraction. We computed methane adsorption isotherms of all structures falling between the two vertical blue lines and having a void fractions between 0.25 and 0.70.

S2 Comparison with experimental data

To test the reliability of our methodology, we compared the methane adsorption isotherms of experimental structures that were available in the literature to the analogous structures in our dataset. Using Grand-canonical Monte Carlo simulations, we simulated the isotherms for HKUST-1 (see Fig. S2); Mg-MOF-74, Ni-MOF-74, and Co-MOF-74 (see Fig. S3); and MOF-5 and PCN-14 (see Fig. S4) from 0 to 80 bar at 298 K.

For PCN-14 and MOF-5, our simulations give a good agreement with the experimental data. For the MOF-74 series, it is known that not all open metal sites are activated [1], giving a lower maximum adsorption compared to the perfect crystal structures used in our simulations. To correct for these blocked adsorption sites, we scaled the isotherms by the ratio of normalized surface areas in Mg-, Co-, and Ni-MOF-74, as reported in Table 2 of Ref. [2], where the surface areas are derived from a Langmuir fit of 77K N_2 adsorption isotherms. In the case of Zn-MOF-74, $\approx$ 24% of the surface area, and thus binding sites, is not accessible; in Ni-MOF-74, $\approx$ 10%; in Mg-MOF-74, $\approx$ 13%; and in Co-MOF-74, $\approx$ 18% of binding sites are not accessible. We see that in frameworks with these particularly strong binding sites, such as Ni-MOF-74 and HKUST-1, the UFF + TraPPE force field underestimates the adsorption isotherms.

In conclusion, our force field tends to slightly underestimate the measured methane uptake in certain materials, by anywhere from 7% (MOF-5) to 20% (Ni-MOF-74) at 65 bar, which explains why in our screening study our top performing structures have a slightly lower deliverable capacity compared to the experimental structures.

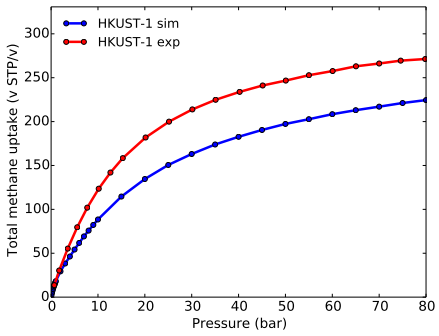

Figure S2. Adsorption isotherm of methane in HKUST-1. The experimental data are from Mason *et al.* [1].

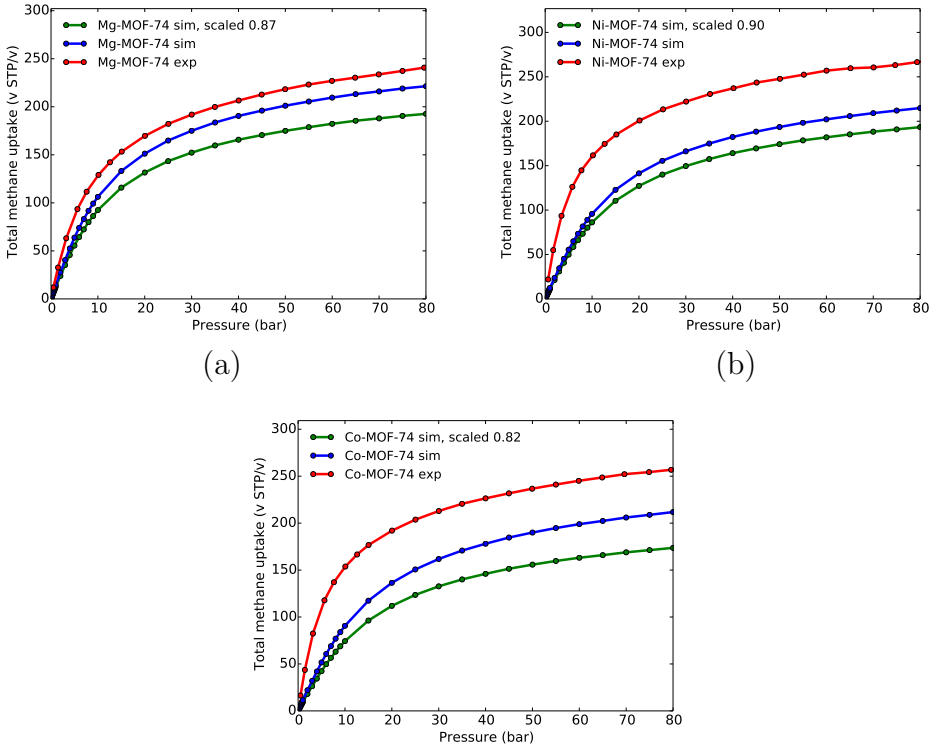

Figure S3. Adsorption isotherm of methane in (a) Mg-MOF-74, (b) Ni-MOF-74, and (c) Co-MOF-74. The experimental data are from Mason *et al.* [1]. The simulated isotherms are scaled to take into account that in the experimental structures not all open metal sites are accessible.

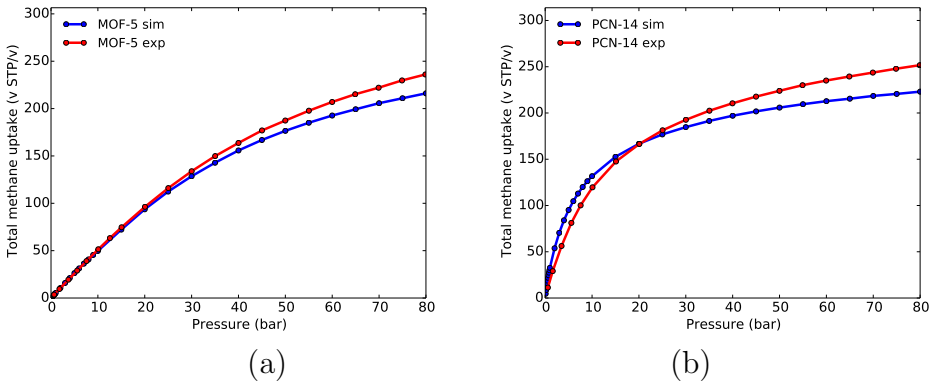

Figure S4. Adsorption isotherm of methane in (a) MOF-5 and (b) PCN-14. The experimental data are from Mason *et al.* [1].

S3 Top material for methane storage

The material with the highest predicted deliverable capacity in our study is a hypothetical porous polymer network (PPN), Adamantane 4387 1-net 004 [3], exhibiting a 65 - 5.8 bar deliverable capacity of 196 v STP/v. The structure is shown in Fig. S5. We plotted the potential energy contours of a methane molecule in the pores at -12 kJ/mol (orange) and 0 kJ/mol (gray) to highlight the binding regions. This material exhibits a largest included sphere of 11.75 $\AA$; this is larger than a single methane molecule. The strong binding regions in orange indicate that multiple methane molecules can be efficiently packed into the pores. The computed surface area of this material is 1992 m^2/cm^3.

This PPN can in principle be synthesized from known synthesis routes [4] using an adamantane core and 1,2-dibromoethylene linkers: Four of these linkers are appended to each tetrahedral point of the adamantane cage. When two of these tetrahedral monomers then react, we get the C_4H_4 linkage spanning the adamantane cages. This 'two-monomer synthesis route' is discussed in detail in Ref. [3].

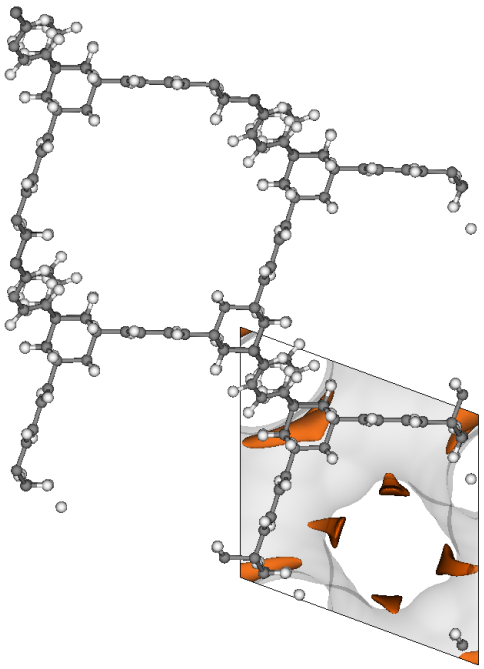

Figure S5. Adamantane 4387 1-net 004 exhibits a 65 - 5.8 bar methane deliverable capacity of 196 v STP/v. Contours of the potential energy of a methane molecule in the pores are shown at -12 kJ/mol (orange) and 0 kJ/mol (gray).

S4 Estimating the saturation loading M

To estimate the saturation methane loading in each material, which we call the effective density of adsorption sites, we fit the simulated methane adsorption isotherms from 1 – 160 bar fugacity to model 1 in Ref. [5], which builds upon a Langmuir model by including adsorbate-adsorbate interactions. The model is a Langmuir model at first order, with a correction term that is weighted by the strength of the adsorbate-adsorbate interactions (θ) [5]

$$\frac{\sigma}{M} = \frac{\frac{K_H}{M}\phi P}{1+\frac{K_H}{M}\phi P} + \theta\left(\frac{\frac{K_H}{M}\phi P}{1+\frac{K_H}{M}\phi P}\right)^2\left(\frac{\frac{K_H}{M}\phi P}{1+\frac{K_H}{M}\phi P} - 1\right). \tag{S1}$$

The variable σ is the methane loading per volume of material; M is the saturation loading or effective density of sites; K_H is the Henry coefficient; P is the pressure; ϕ is the fugacity coefficient such that ϕP is the fugacity of methane corresponding to pressure P. The Henry coefficient in eqn S1 is independently obtained from the Widom insertion method. We thus fit each methane adsorption isotherm to the model in eqn S1 using the parameters M and θ with a nonlinear least squares data fitting routine implemented with the OPTIMIZE function in Scipy, an open-source computing package in Python. If the highest-pressure point in the simulated isotherm (160 bar fugacity) was less than 60% of the identified M, we extended the isotherms to a fugacity of 700 bar to obtain enough curvature in the simulated isotherms for our fitting routine to reliably estimate M. For plots involving M, we only include structures whose residual sum of squares (including all 14 data points on the isotherm) is below 5% of M to help ensure the estimation of M is reliable.

S5 Literature survey for experimental methane adsorption isotherms

We searched the literature for high-performing structures in each material class for which experimentally measured methane adsorption isotherms were available. Where noted, we took the total adsorption; otherwise, we converted the excess adsorption into total using the reported pore volume and the density of methane from the Peng-Robinson equation of state. These data are depicted in Fig. 4 of the main text.

The model in eqn S1 was fitted to the experimental adsorption isotherms to interpolate methane adsorption for the relevant pressures when the experimental measurement was not taken at exactly 5.8 and 65 bar. The experimental data were taken from the following references: MOF-519 and MOF-520 [6]; HKUST-1, Mg2(dobdc), Ni2(dobdc), MOF-5, PCN-14 [1]; IRMOF-6 [7]; PCN-16, [8]; NU-125, UTSA-20 [9]; ZIF-8, ZIF-76, [10]; PPN-4 [11]; PPN-1, PPN-2, PPN-3 [12]; DD3R [13]; and Silicate for crystal density [14].

S6 Alternative Operating Conditions

Here, we outline our methods for calculating the deliverable capacity of our materials under different conditions than set in the ARPA-E target. To avoid having to carry out simulations at many different temperatures and pressures, we characterize each material by the parameters M, K_H, and θ obtained from fitting the simulated isotherms at 298 K to the model in eqn S1. To extrapolate the loading at a higher temperature, we assume that the temperature dependence of the Henry coefficient K_H is given by the Van't Hoff equation and the temperature dependence of θ (see Ref. [5]):

$$K_H \sim e^{-\frac{\Delta H}{RT}} \tag{S2}$$

$$\theta \sim \frac{1}{T}. \tag{S3}$$

We calculated the enthalpy of adsorption ΔH (= negative of the heat of adsorption) during our simulations. We subsequently use these parameters to estimate the methane adsorption at alternative conditions.

To test that the various predictions made with these fitted parameters gives a sufficiently accurate description of the isotherms that would be obtained by simulations we carried out several tests. In Fig. S6 we show that the fitted isotherms describe the simulated deliverable capacity sufficiently accurate. Fig. S7 shows that this approach gives a sufficiently accurate description of the methane adsorption isotherms at these different temperatures.

S6.1 Altering the operation conditions

In the calculations that follow, we include a random sample of 3,701 materials from each class to assign each class an equal prior. We amalgamate all material classes together and plot the distribution of deliverable capacities at the different storage conditions. For each alternative operating condition, we also depict how one class of materials may perform better over another class at different conditions by stacking the probability distributions for each class. This allows us to visualize the contributions of each material class to the probability distributions.

We now assess the impact of changing the operating pressures on the deliverable capacity at 298 K. Methane is stored in the adsorbed natural gas tank at P_H bar at the refilling station, and a tank is considered depleted if it exhibits a pressure of P_L bar. By changing P_H and P_L, we compute the deliverable capacity under two scenarios that will benefit the deliverable capacity: (i) Increasing the storage pressure P_H but keeping the ARPA-E target's discharge pressure of $P_L = 5.8$ bar (ii) Decreasing the discharge pressure P_L but keeping the ARPA-E target's storage pressure of $P_H = 65$ bar.

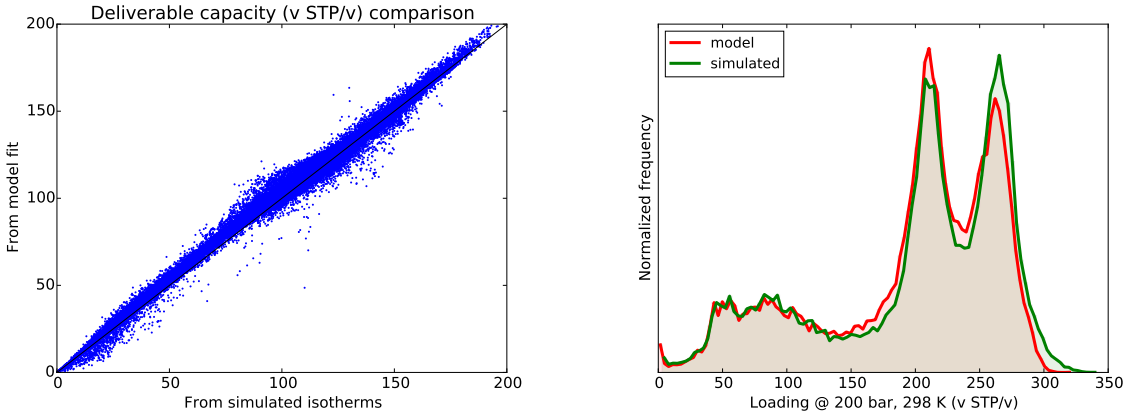

(a) (b)

Figure S6. Validating the approximation of isotherms with the model in eqn. S1. (a) For each material, we plotted the deliverable capacities at 298 K between 65 and 5.8 bar obtained from the model fit against that obtained from the simulated isotherm. The points follow the diagonal with a modest variance. (b) We compare the distribution of 200 bar loadings using the simulated loading and the fitted model.

S6.1.1 Altering the storage pressure

Fig. S8 shows how the distribution of deliverable capacities is changing if we increase the storage pressure P_H = 65, 100, 150, and 200 bar. As expected, the higher the storage capacity the larger the deliverable capacity; however, even at 200 bar we do not reach the ARPA-E target.

S6.1.2 Altering the decharging pressure

Fig. S9 shows the effects of decreasing the recharging pressure P_L = 5.8, 3, 1, and 0 bar, while keeping the charging pressure P_H = 65 bar. In these calculations the deliverable capacity with $P_L = 0$ is equal to the loading at P_H = 65 bar. As expected, decreasing the decharging pressure increases the deliverable capacity. In particular materials for which methane is strongly bound will have a higher deliverable capacity.

S6.1.3 Heat rerouting deliverable capacity

In the main text, we investigate the strategy of rerouting waste heat from the engine to the adsorbent when the tank nears discharge, driving off the residual methane, thereby increasing the deliverable capacity. The heat-rerouting deliverable capacity given a heating temperature of T_f is then:

$$\sigma(P_H, T_0) - \sigma(P_L, T_f), \tag{S4}$$

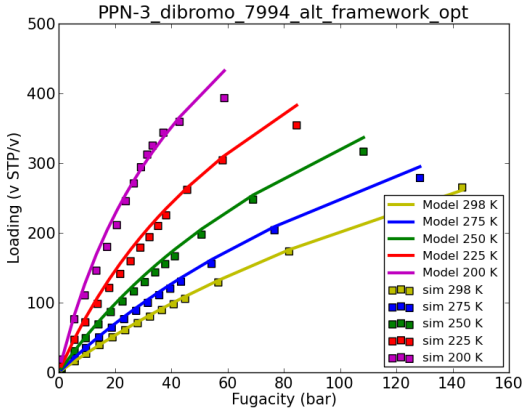

(a)

Figure S7. Methane adsorption isotherms calculated for a sample structure with simulations (points) against the extrapolations from the model in eqn S1 that was fit to the 298 K isotherm (solid lines) for varying temperatures.

where the loading $\sigma(P,T)$ is given by the model in eqn S1 and the scalings in eqn S3 are taken into account for the second term. We took into account the temperature-dependence of the fugacity through the Peng-Robinson equation of state.

Fig. S10 shows the heat-rerouting deliverable capacity distributions broken down into material classes for $T_f = 400$ K in comparison to the isothermal deliverable capacity considered by ARPA-E. Also shown is the extreme limit of exploiting the temperature-dependence of the isotherms: at best, this heat-rerouting strategy will drive off all residual methane gas at the discharge, and the heat-rerouting deliverable capacity becomes the loading at P_H as $T_f \to \infty$. In none of these scenarios do we reach the ARPA-E target.

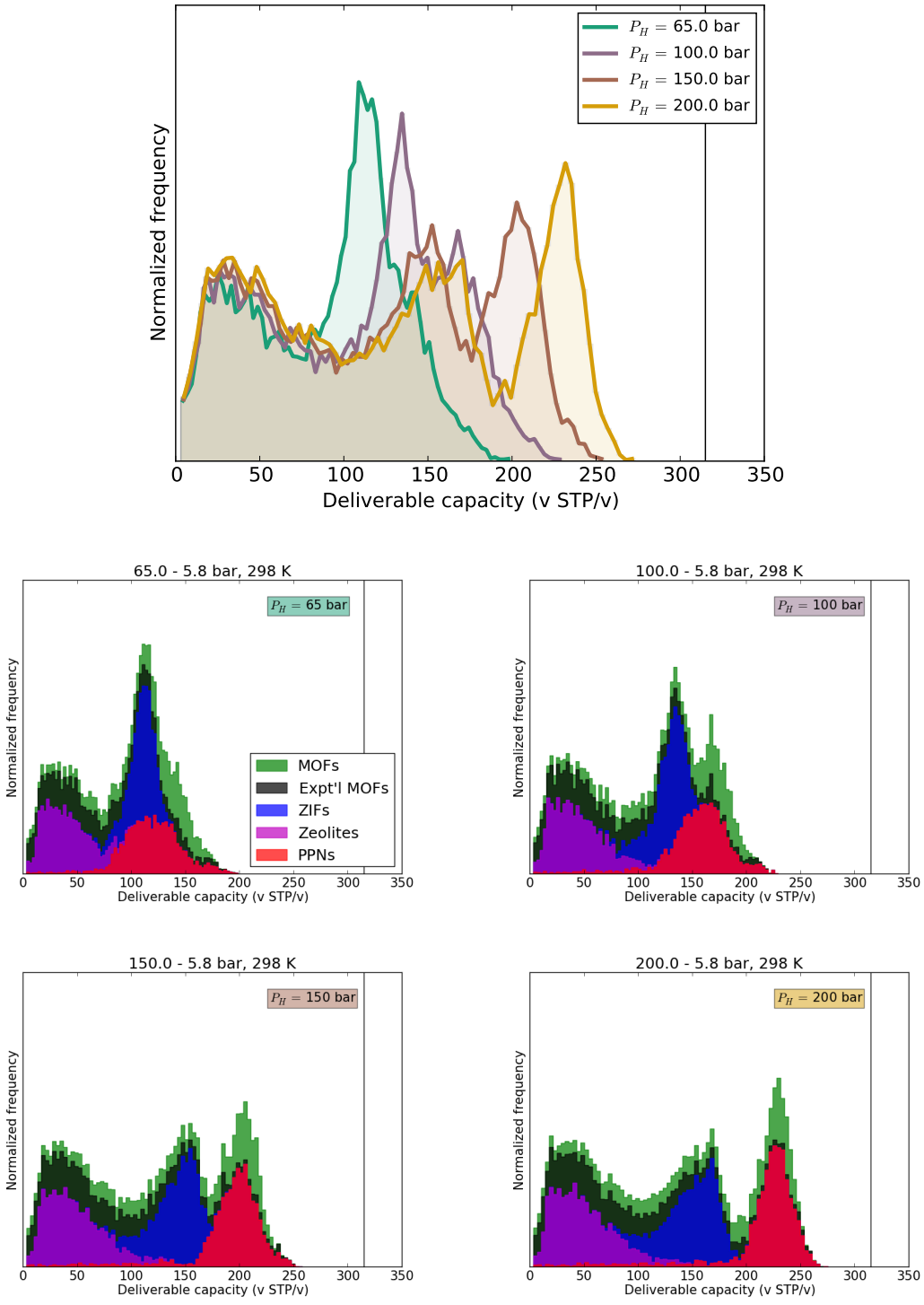

Figure S8. Changing the storage pressure: deliverable capacity of methane for materials operating between pressure P_H and 5.8 bar. [Top] Deliverable capacity distributions under differing P_H. [Bottom] For each scenario, the distribution is partitioned into material classes. The vertical line is the ARPA-E target.

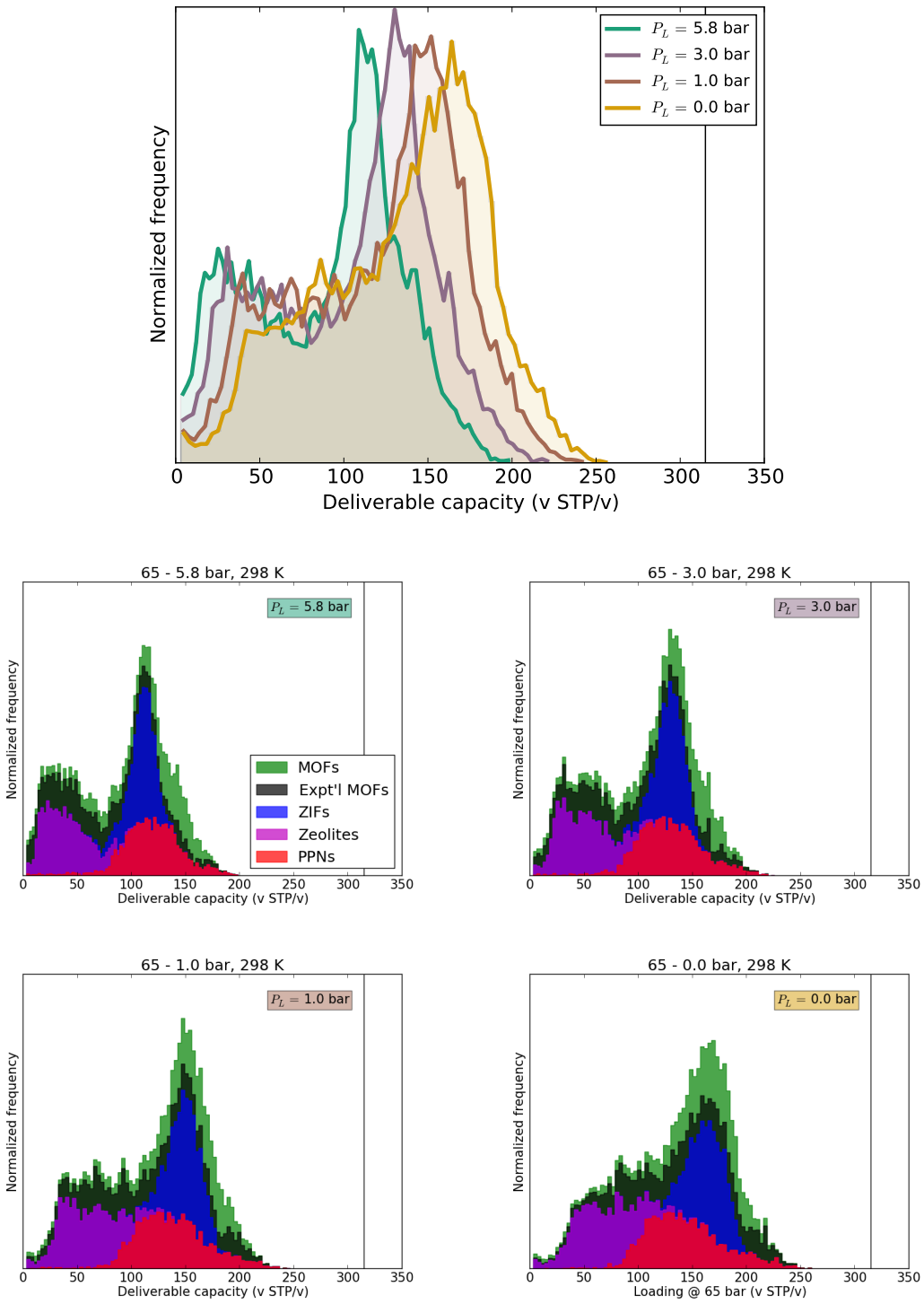

Figure S9. Changing the discharge pressure: deliverable capacity of methane for materials operating between pressure 65 and P_L bar. [Top] Deliverable capacity distributions under differing P_L. [Bottom] For each scenario, the distribution is partitioned into material classes. The vertical line is the ARPA-E target.

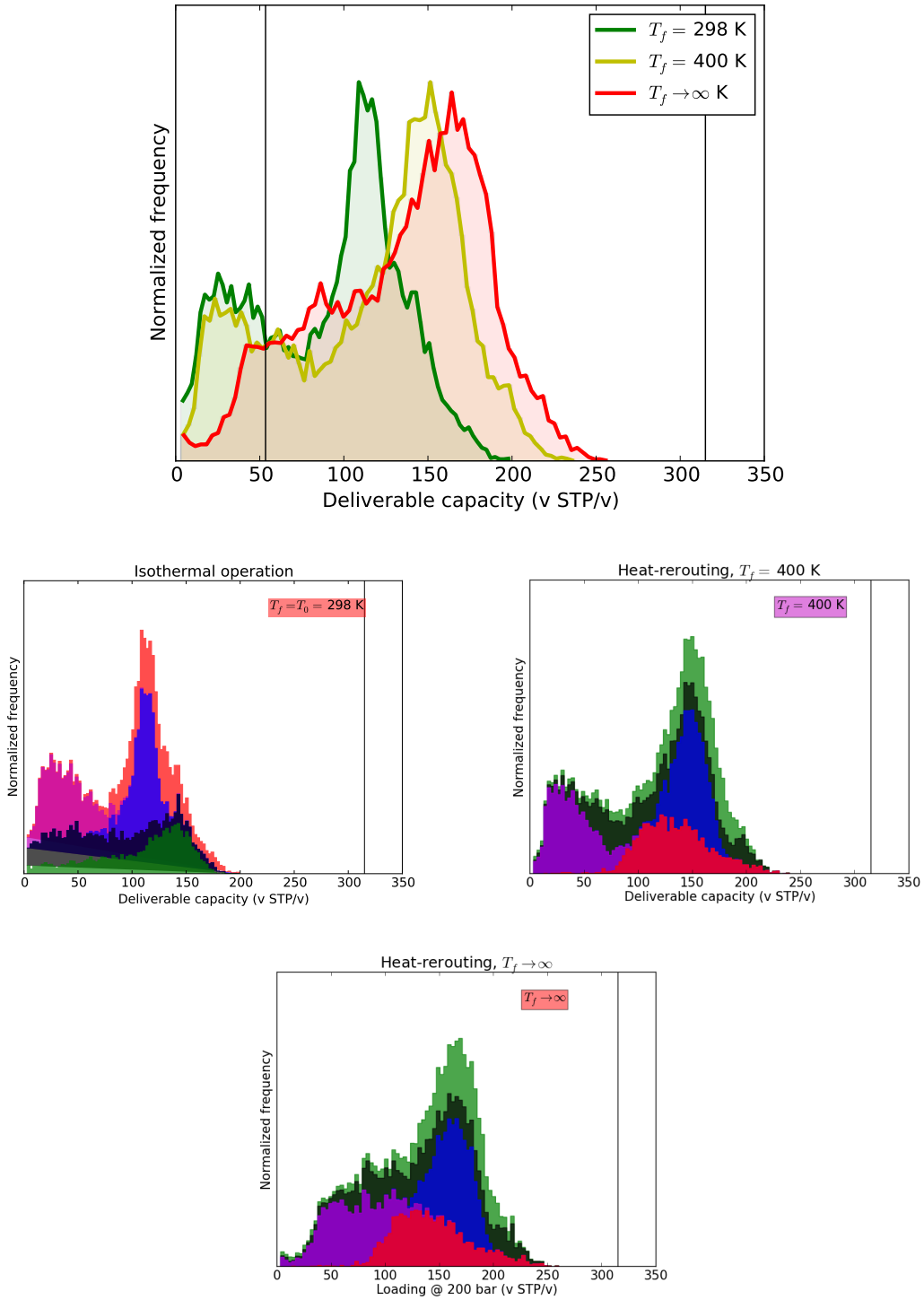

Figure S10. Heat-rerouting deliverable capacity. [Top] Heat-rerouting deliverable capacity where the adsorbent is heated to a temperature T_f when the tank nears discharge. [Bottom] For each scenario, the distribution is partitioned into material classes. The vertical line is the ARPA-E target.

S7 Additional data

In the main text, Fig. 4 shows the relationship between the deliverable capacity and the crystal density. In Fig. S11 we reproduce the same figure but now color-coded by the fractional deliverable capacity. This figure illustrates that (i) the materials with the highest deliverable capacities also have the highest fractional deliverable capacities, and (ii) a high fractional deliverable capacity does not necessarily translate to a high deliverable capacity.

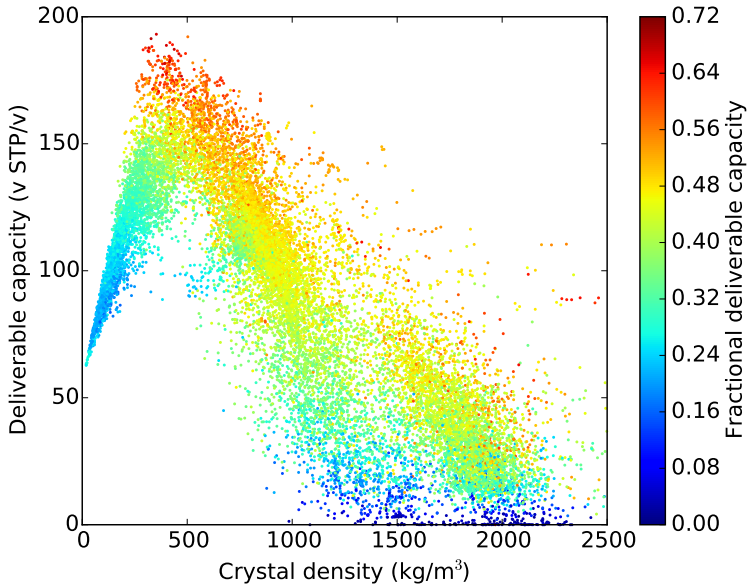

Figure S11. Materials with the highest deliverable capacities indeed have the highest fractional deliverable capacities. Deliverable capacity plotted against the crystal density. Points are color-coded according to fractional deliverable capacity.

In Fig. 5 of the main text, we plotted the fractional deliverable capacity against the saturation loading of all materials in one figure. In Fig. S12, we present this plot separately for each class of material. In addition, the dashed horizontal line marks the theoretical upper bound if a material would be described with a Langmuir isotherm [5]. Above this theoretical upper bound, we find materials that cannot be described with a Langmuir isotherm due to, for example, methane-methane interactions.

Fig. S13 gives the diameter of the largest included sphere as a function of the crystal density.

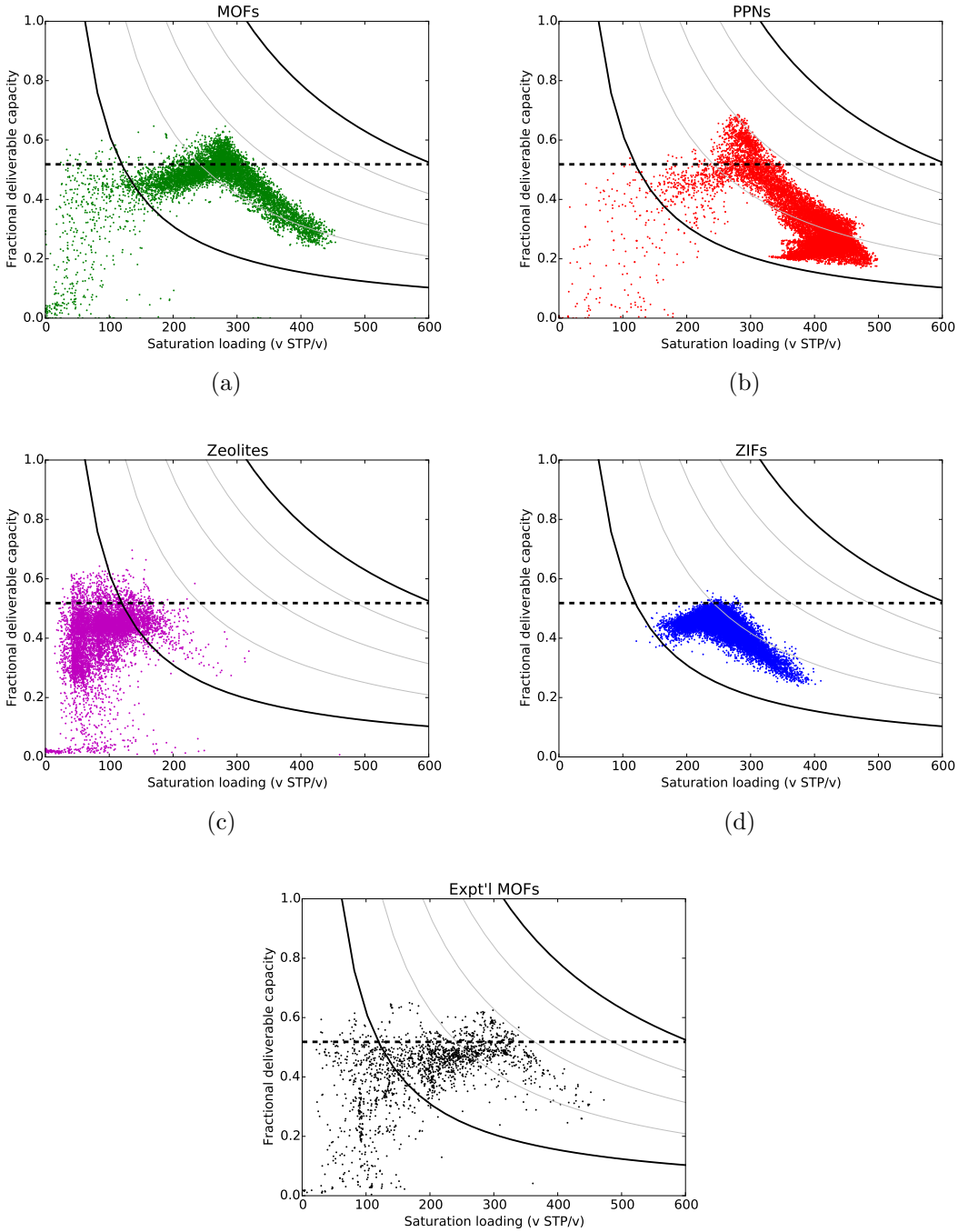

Figure S12. Fractional deliverable capacity f plotted against density of sites M (saturation loading). Curves are lines of constant deliverable capacity: bottom bold curve is that of a free space tank (62 v STP/v) and top bold curve is the ARPA-E target. Region exceeding ARPA-E target is highlighted in yellow. (a) MOFs, (b) PPNs, (c) zeolites, (d) ZIFs, and (e) Experimental MOFs. Horizontal, dashed line is optimal fractional deliverable capacity for a Langmuir model as calculated by eqn. 6 of Ref. [15].

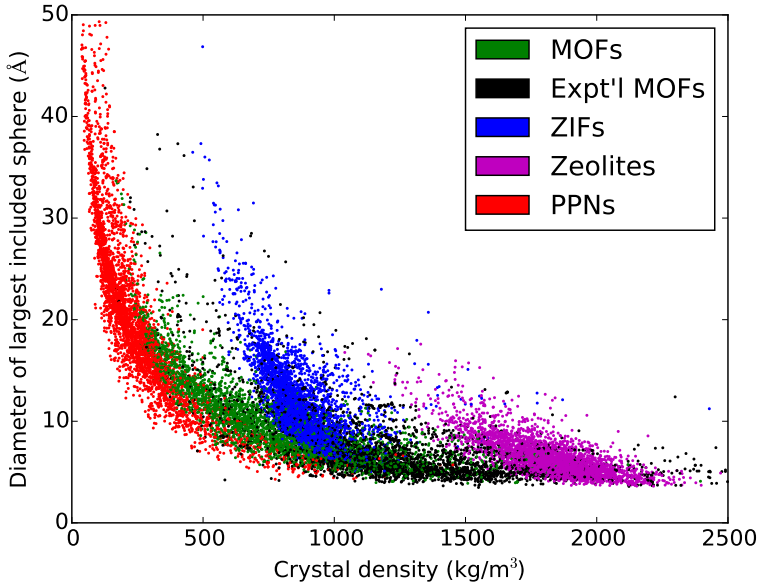

Figure S13. Crystal density correlates with pore size. The diameter of the largest included sphere is plotted against the crystal density. Each point is a structure color-coded by material class.

References

1. J. A. Mason, M. Veenstra, and J. R. Long, "Evaluating metal–organic frameworks for natural gas storage," *Chemical Science*, vol. 5, no. 1, pp. 32–51, 2014.

2. W. Queen, M. Hudson, E. Bloch, J. A. Mason, M. Gonzalez, J. Lee, D. Gygi, J. Howe, K. Lee, T. Darwish, M. James, V. K. Peterson, S. Teat, B. Smit, J. Neaton, J. R. Long, and C. M. Brown, "Comprehensive study of carbon dioxide adsorption in the metal-organic frameworks m2(dobdc) (m = mg, mn, fe, co, ni, cu, zn)," *Chem. Sci.*, 2014.

3. R. L. Martin, C. Simon, M. Haranczyk, and B. Smit, "In silico design of porous polymer networks: high-throughput screening for methane storage materials," *Journal of the American Chemical Society*, 2014.

4. M. Rose, W. Böhlmann, M. Sabo, and S. Kaskel, "Element–organic frameworks with high permanent porosity," *Chemical Communications*, no. 21, pp. 2462–2464, 2008.

5. C. M. Simon, J. Kim, L.-C. Lin, R. L. Martin, M. Haranczyk, and B. Smit, "Optimizing nanoporous materials for gas storage," *Physical Chemistry Chemical Physics*, vol. 16, pp. 5499–5513, 2014.

6. F. Gndara, H. Furukawa, S. Lee, and O. M. Yaghi, "High methane storage capacity in aluminum metal-organic frameworks," *Journal of the American Chemical Society*, vol. 136, no. 14, pp. 5271–5274, 2014.

7. M. Eddaoudi, J. Kim, N. Rosi, D. Vodak, J. Wachter, M. O'Keeffe, and O. M. Yaghi, "Systematic design of pore size and functionality in isoreticular MOFs and their application in methane storage," *Science*, vol. 295, no. 5554, pp. 469–472, 2002.

8. D. Sun, S. Ma, J. M. Simmons, J.-R. Li, D. Yuan, and H.-C. Zhou, "An unusual case of symmetry-preserving isomerism," *Chemical Communications*, vol. 46, no. 8, pp. 1329–1331, 2010.

9. Y. Peng, V. Krungleviciute, I. Eryazici, J. T. Hupp, O. K. Farha, and T. Yildirim, "Methane Storage in MetalOrganic Frameworks: Current Records, Surprise Findings, and Challenges," *Journal of the American Chemical Society*, vol. 135, no. 32, pp. 11887–11894, 2013.

10. J. Pérez-Pellitero, H. Amrouche, F. R. Siperstein, G. Pirngruber, C. Nieto-Draghi, G. Chaplais, A. Simon-Masseron, D. Bazer-Bachi, D. Peralta, and N. Bats, "Adsorption of CO2, CH4, and N2 on zeolitic imidazolate frameworks: experiments

and simulations," *Chemistry-A European Journal*, vol. 16, no. 5, pp. 1560–1571, 2010.

11. D. Yuan, W. Lu, D. Zhao, and H.-C. Zhou, "Highly stable porous polymer networks with exceptionally high gas-uptake capacities," *Advanced Materials*, vol. 23, no. 32, pp. 3723–3725, 2011.

12. W. Lu, D. Yuan, D. Zhao, C. I. Schilling, O. Plietzsch, T. Muller, S. Brase, J. Guenther, J. Blumel, R. Krishna, *et al.*, "Porous polymer networks: synthesis, porosity, and applications in gas storage/separation," *Chemistry of Materials*, vol. 22, no. 21, pp. 5964–5972, 2010.

13. S. Himeno, T. Tomita, K. Suzuki, and S. Yoshida, "Characterization and selectivity for methane and carbon dioxide adsorption on the all-silica DD3R zeolite," *Microporous and Mesoporous Materials*, vol. 98, no. 1, pp. 62–69, 2007.

14. E. Flanigen, J. Bennett, R. Grose, J. Cohen, R. Patton, R. Kirchner, and J. Smith, "Silicalite, a new hydrophobic crystalline silica molecular sieve," *Nature*, vol. 271, pp. 512–516, 1978.

15. K. R. Matranga, A. L. Myers, and E. D. Glandt, "Storage of natural gas by adsorption on activated carbon," *Chem. Eng. Sci.*, vol. 47, no. 7, pp. 1569 – 1579, 1992.